

# A Low-Cost Portable 50 mT MRI Scanner for Dental Imaging

Xiaohan Kong (孔晓涵)<sup>1</sup>, Yaomin Zhu (朱耀旻)<sup>2</sup>, Sheng Shen (沈晟)<sup>3</sup>, Jiamin Wu (吴嘉敏)<sup>4</sup>,  
Yucheng He (贺玉成)<sup>5</sup>, Mingjian Hong (洪明坚)<sup>6</sup>, and Zheng Xu (徐征)<sup>7</sup>

**Abstract**—Magnetic resonance imaging (MRI) has proven excellent performance in dental imaging, especially for temporomandibular joint (TMJ), teeth, and periodontal apparatus; however, the high price and strict installation environment of the conventional high-field MRI has prevented its widespread use in dental clinics or developing regions. The introduction of low-cost and portable MRI scanners will help increase the easy accessibility of MRI examinations and reduce the patients' waiting time. This work introduces a low-cost portable 50 mT MRI scanner for dental imaging. First, the overall structure, including permanent magnets, gradient coils, and radio frequency (RF) coils, is introduced. The cooling system is removed because the static field is maintained by the permanent magnets. The system stands 90 cm wide and 110 cm high and weighs 600 kg, which makes it possible to install in an average-sized room. Then, the design processes of specialized RF receiving coils for TMJ teeth are illustrated. In order to improve patient comfort, an intraoral wireless coil for boosting the signal-to-noise ratio (SNR) inside the oral cavity is proposed; furthermore, the  $T_1$ -weighted images of TMJ and teeth are given to show the dental imaging performance of the proposed device.

**Index Terms**—Biomedical equipment, biomedical imaging, dental imaging, electromagnetic fields, magnetic resonance imaging (MRI), medical diagnosis, optimization methods, radio frequency (RF).

## I. INTRODUCTION

**D**ENTAL diagnostic imaging typically relies on X-ray-based methods, which have several drawbacks and limitations, including exposure to ionizing radiation, heightened risk of cancer, and incapacity to image soft tissues.

Manuscript received 15 March 2023; revised 10 September 2023; accepted 18 October 2023. Date of publication 1 November 2023; date of current version 29 February 2024. This work was supported in part by the National Natural Science Foundation of China under Grant 52077023, in part by the Shenzhen Science and Technology Innovation Commission under Grant CJGJZD20200617102402006, and in part by the Shenzhen Foundation of Science and Technological Innovation under Grant JCYJ20200109114006014. The Associate Editor coordinating the review process was Dr. Zhen Ren. (Corresponding authors: Zheng Xu; Yaomin Zhu.)

Xiaohan Kong and Zheng Xu are with the School of Electrical Engineering, Chongqing University, Chongqing 400044, China (e-mail: xuzheng@cqu.edu.cn).

Yaomin Zhu is with the Shenzhen Stomatology Hospital, Shenzhen 518000, China (e-mail: zymin555@hotmail.com).

Sheng Shen is with the Massachusetts General Hospital/Martinos Center and Harvard Medical School, Boston, MA 02129 USA.

Jiamin Wu and Yucheng He are with the Shenzhen Academy of Aerospace Technology, Shenzhen 100048, China.

Mingjian Hong is with the School of Software Engineering, Chongqing University, Chongqing 400044, China.

Digital Object Identifier 10.1109/TIM.2023.3329089

Recently, magnetic resonance imaging (MRI) has shown irreplaceable potential in dental diagnosis [1], [2], [3], [4], due to its nonionizing radiation and excellent soft tissue contrast. Dental MRI has been used in a variety of situations, such as imaging of the morphology and function of the temporomandibular joint (TMJ), presurgical and implant planning, and tumor detection [5], [6], [7]. In a radiation-free way, MRI offers exceptional spatial and contrast resolution. Additionally, MRI was recognized as the gold diagnosis standard for joint effusion and TMJ disk-related illness [8]. Regular dental MRI (1.5 or 3 T) provides high-quality images, while the high maintenance price, strict cooling, and shielding requirements limit its availability in dental clinics and developing regions. Low-field MRI has demonstrated its advantages in the diagnosis of human brain stroke and other diseases [9], [10], [11], [12]. Generally, “low-field” is used to broadly describe devices below 1.5 T. A widely accepted definition [13] classifies devices with a main magnetic field strength ranging between 0.01 and 0.1 T as “very low-field (VLF) MRI.” Because of the use of permanent magnets to establish the main magnetic field, VLF MRI equipment does not require a cooling system. In addition, the use of active noise cancellation technology allows the device to be used without shielding. These features make the VLF MRI light, portable, and inexpensive. It can be used in dental clinics or in arbitrary rooms, helping to reduce the cost and waiting time for patients. Nevertheless, the application of VLF MRI devices in dental imaging has seldom been reported. Dental MRI requires a higher resolution and signal-to-noise ratio (SNR) to enable imaging of fine structures. This is a challenge for VLF MRI, which has an inherently low SNR due to its low static magnetic field.

The radio frequency (RF) coil is a key device in transmitting the RF excitation and receiving the nuclear magnetic resonance (NMR) signal. Its properties strongly depend on the object to be imaged. When it comes to TMJ imaging, its proximity to the facial surface makes it an ideal scenario for surface coil imaging. Surface coil design for high field [14], [15], [16] has been studied in many works. The conventional high-field surface coil configuration, however, cannot be applied to VLF MRI directly due to the substantial disparity in operating frequency. For VLF MRI, the impedance of the RF surface coil dominates the SNR, and the interturn distance, the number of turns, and the radius of the coil all need to be optimized. Here, we have reported on a specialized RF coils design

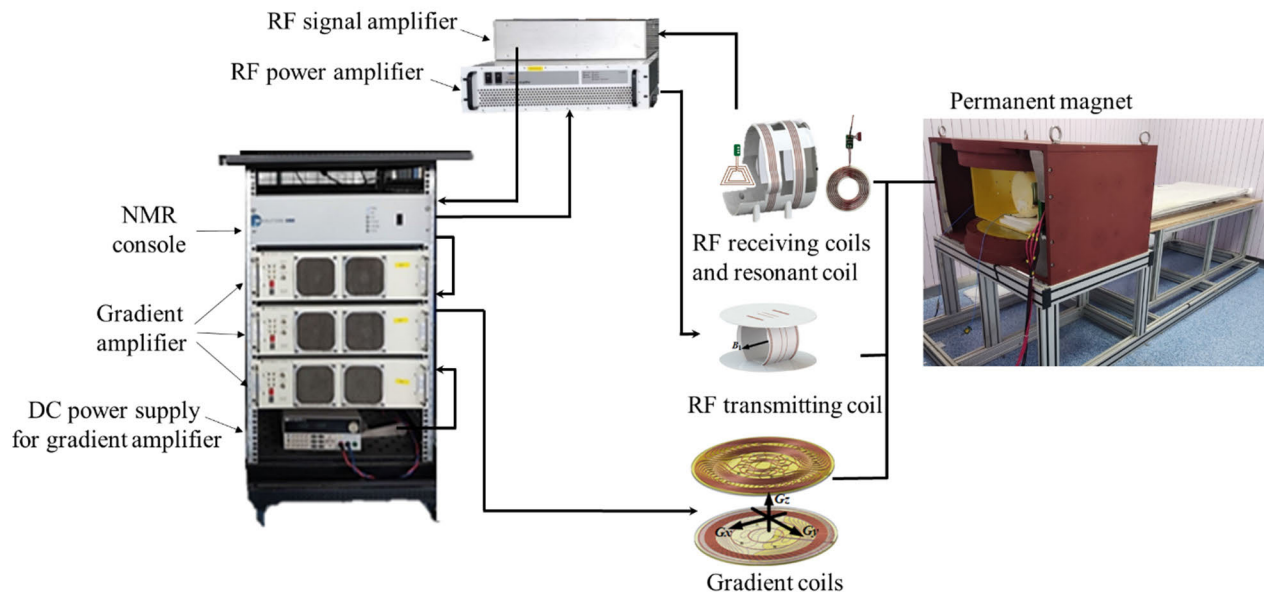


Fig. 1. Overall structure of VLF MRI system.

method for dental TMJ imaging, taking into account the goal of optimizing SNR and field of view (FOV) simultaneously.

Teeth MRI requires high resolution to visualize precise anatomical details. On the one hand, the image resolution depends on both the FOV and the size of the reconstruction matrix. A smaller FOV is preferred because increasing the FOV increases the scan time to achieve the desired image resolution at a similar SNR [17]. On the other hand, the acquired FOV must include the entire sensitive volume of the RF coil to avoid aliasing; therefore, it is imperative to use smaller and more localized RF coils to achieve higher resolution within a reasonable scan time. In teeth imaging, there are two main types of coils used: extraoral coils and intraoral coils, which are placed inside and outside the mouth, respectively. For extraoral coils [18], the large distance between the coil and the teeth can result in lower sensitivity and a strong undesired signal from surrounding tissues like the cheek and oral fat. These undesired signals can dominate over the signal from the region of interest (ROI) and create difficulties in visualizing the desired structures. To overcome these limitations, intraoral coils [19], [20], [21], [22] have been proposed to increase both resolution and SNR by reducing interference from surrounding tissues. For better convenience of use and to reduce the cost of coil production, a wireless resonant coil is used instead of a wired intraoral receiver coil. Wireless resonant coils offer the advantage of greater patient comfort and ease of placement as they do not require the use of wires. This can make the imaging process more streamlined and convenient while reducing the cost of coil production.

The study reports the overall structure of a VLF MRI system for dental imaging, particularly for TMJ and teeth. The surface coil optimization method is discussed for TMJ imaging to improve the SNR. A wireless resonant coil is introduced as an intraoral coil that has the potential to improve local SNR and overcome the limitations of wired RF surface coils. Imaging experiments are conducted both on phantom and in vivo, and

the results are presented in the form of images of the TMJ, teeth and periodontal apparatus of volunteer subjects. These images serve as a testament to the capabilities of the system in the field of dental imaging. Finally, we compare the imaging results with those of high-field imaging and discuss the pros and cons brought about by portability.

## II. OVERALL STRUCTURE OF VLF MRI DEVICES

The overall structure of the VLF MRI system is shown in Fig. 1. The total weight of the system is around 600 kg, with a spherical effective imaging area of 200 mm in diameter. Permanent magnet, RF excitation coil, RF receiving coil and gradient coils compose the main device body. The signal excitation and processing system consists of several components, including RF signal amplifiers, an NMR console, a gradient amplifier, and a dc power supply for gradient amplifiers. Detailed parameters of these parts are given as follows:

- 1) *Permanent Magnet*: It generates a uniform static background field along vertical direction, and is constructed using samarium cobalt (SmCo) with a composition of SmCo30H. The average magnetic field strength in the ROI (sphere with a diameter of 200 mm) is about 50 mT, with a nonuniformity of less than 200 ppm. These field measurements were conducted with a Metrolab Precision NMR Tesla meter (PT2026, resolution: 0.01 ppm in uniform 3 T field, accuracy:  $\pm 5$  ppm of field strength).
- 2) *RF Excitation and Receiving Coil*: The RF excitation coil generates RF pulses and delivers these pulses to the human tissue. This NMR signal generated by the excited nuclei in the imaged tissue is then received by the RF receiving coil and processed by the NMR console to create an image. The RF excitation coil comprises two pairs of opposing solenoidal coils, producing an RF excitation field with a uniformity of less than 5% in ROI. The operational frequency is 2.32 MHz. The receiving

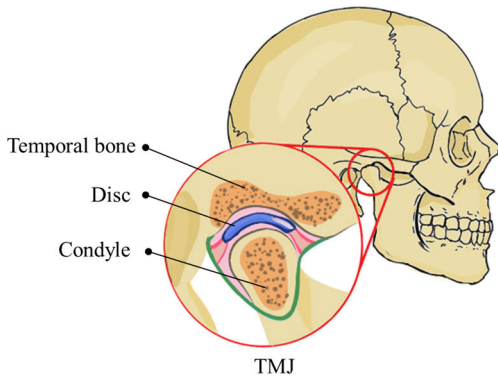


Fig. 2. Anatomical structure of TMJ.

coil consists of the head coil, surface coil, and resonant coil components, which will be described later.

- 3) *Gradient Coils*: Gradient coils create linear gradient fields in three directions, allowing the creation of MRI images with spatial resolution. The maximum nonlinearity is 4.5% ( $X/Y$  gradient coil) and 3.2% ( $Z$  gradient coil), and efficiency is  $242 \mu\text{T}/(\text{m}\cdot\text{A})$  ( $X/Y$  gradient coil) and  $274 \mu\text{T}/(\text{m}\cdot\text{A})$  ( $Z$  gradient coil).
- 4) The RF power amplifier (BT00250-AlphaS, TOMCO) and RF signal amplifier (lab-made) are used to supply the required power for RF excitation coil and amplify the NMR signals received by the RF receiving coil, respectively.
- 5) The NMR console (EVO, MR SOLUTIONS) is responsible for executing the pulse sequences, generating the RF and gradient signals, detecting the NMR signals, and processing the data to construct the final images.
- 6) The gradient amplifier (CA-150 SERIES, PCI) is powered by adc power supply (IT6724, ITECH), providing the power to generate the gradient magnetic field.

### III. RF COIL DESIGN FOR TMJ IMAGING

#### A. Design Target

The TMJ is the joint connecting the skull and mandible and is located in front of the ear. The depth of the TMJ is typically a few centimeters below the skin surface, making it accessible to imaging with surface RF coils. Surface coils are known for their high SNR in close proximity to the coil surface. The anatomical structure of the TMJ is shown in Fig. 2. In the case of TMJ disorder, the main diagnostic criteria rely on the position and shape of the disk [7].

The design of the surface coil takes into consideration the average size and depth of the TMJ to ensure optimal performance. The aim is to maximize the SNR in the target area with a diameter of 30 mm and a depth of 30–40 mm from the skin surface. The structure of the surface coil directly affects the SNR, and thus, its optimization is crucial for achieving images of the TMJ. The SNR has the following relationship [23]:

$$\text{SNR} \propto \frac{B_1}{\sqrt{R}} \quad (1)$$

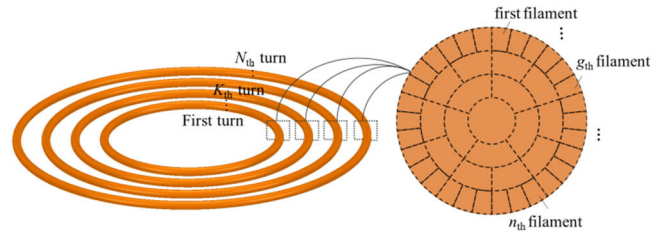
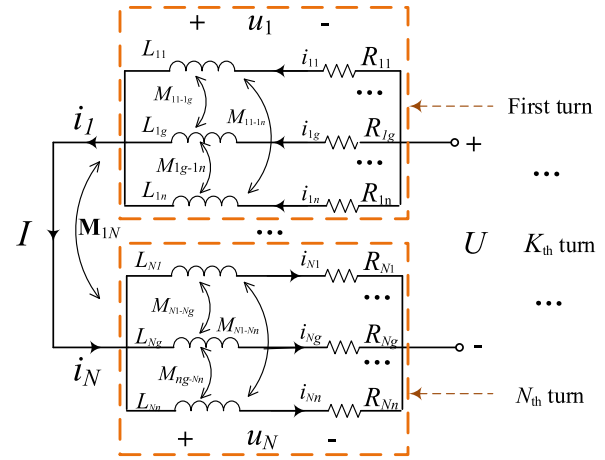
Fig. 3. Discretization strategy of simplified PEEC method. The left is an  $N$ -turn surface coil, and the right conductor shows the meshing details on the cross section of one single turn of the coil.

Fig. 4. Equivalent circuit diagram of the coil in simplified PEEC method.

where  $B_1$  denotes the effective RF magnetic field, which is the component of the RF magnetic field that is perpendicular to the static magnetic field.  $R$  is the equivalent ac resistance of the RF coil, which is influenced by the skin and proximity effect in working frequency. The traditional approach of using wire length as an indicator of ac resistance ( $R$ ) [24] is not accurate, as it does not take into account the eddy current effects. In this study, a simplified partial element equivalent circuit (PEEC) method [25], [26] is proposed for the calculation of  $R$  and  $B_1$ , which reduces computation time compared to finite element method (FEM) calculations. The PEEC method converts the electromagnetic field problem into a circuit domain and considers the resistance changes caused by eddy currents. The computation time for a single surface coil is only about two seconds with this method when using AMD Ryzen7 5800H at 3.20 GHz with a memory of 64 GB.

#### B. SNR Calculation

First, we introduce the simplified PEEC method to fast calculate the ac resistance ( $R$ ). An  $N$ -turn surface coil is shown in Fig. 3. The cross section of each turn is then meshed with the  $n$  filament's circular loops. To account for the skin effect, we used a nonequidistant mesh with a coarser density toward the interior and a finer density near the surface where the current is denser.

Fig. 4 shows the equivalent circuit diagram, in which every filament loop in Fig. 3 is represented by the lumped circuit components. The influence of capacitance was overlooked because the RF operating frequency is at around 2.3 MHz,

and the capacitance effect has a negligible impact on the coil impedance [27]. Branches in the orange dashed box represent the  $n$  filament's loops connected in parallel in the  $K_{\text{th}}$  turn, which are cascaded with the remaining  $(N - 1)$  turns. Taking the  $N_{\text{th}}$  turn as an example,  $u_N$  and  $i_N$  are the voltage and current of the  $N_{\text{th}}$  turn, and  $R_{N_g}$ ,  $L_{N_g}$ , and  $i_{N_g}$  are the dc resistance, self-inductance, and current, respectively, of the  $g_{\text{th}}$  filament that belongs to the  $N_{\text{th}}$  turn.  $M_{N1-N_g}$  is the mutual inductance between the first filament of the  $N_{\text{th}}$  turn and the  $g_{\text{th}}$  filament of the  $N_{\text{th}}$  turn. Because the cross section of each filament is so small the current is assumed to be uniformly distributed, and  $R_{N_g}$  can be calculated as the dc resistance using the formula as follows:

$$R_{N_g} = \frac{\rho l_{N_g}}{S_{N_g}} \quad (2)$$

where  $\rho$  depicts the resistivity,  $l_{N_g}$  and  $S_{N_g}$  represent the circumference and cross-sectional area, respectively, of the filament. The mutual inductance [28]  $M_{N1-N_g}$  can be calculated as

$$M_{N1-N_g} = \mu_0 \sqrt{r_{N1} r_{N_g}} \left[ \left( \frac{2}{k} - k \right) K(k) - \frac{2}{k} E(k) \right] \quad (3)$$

$$k^2 = \frac{4r_{N1} r_{N_g}}{(r_{N_g}^2 + r_{N_g}^2) + \Delta z^2} \quad (4)$$

where  $r_{N1}$  and  $r_{N_g}$  are the radius, respectively, of two filament loops and  $\Delta z$  is their relative distance in the  $z$ -direction.  $K$  and  $E$  are the complete elliptic integrals of the first kind and  $\mu_0$  is the permeability of the vacuum. The self-inductance of filament loop  $L_{N_g}$  can be attained via formula (3) when  $r_{N1} = r_{N_g}$  and  $\Delta z = 0$ .

According to the equivalent circuit diagram shown in Fig. 4, The equivalent matrix equation is established as

$$\begin{bmatrix} \mathbf{U}_1 \\ \vdots \\ \mathbf{U}_K \\ \vdots \\ \mathbf{U}_N \end{bmatrix} = \begin{bmatrix} \mathbf{R}_1 + jw\mathbf{M}_{11} \cdots jw\mathbf{M}_{1K} \cdots jw\mathbf{M}_{1N} & & \\ & \ddots & \\ jw\mathbf{M}_{K1} \cdots \mathbf{R}_K + jw\mathbf{M}_{KK} \cdots jw\mathbf{M}_{KN} & & \\ & \vdots & \\ jw\mathbf{W}_{N1} \cdots jw\mathbf{W}_{NK} \cdots \mathbf{R}_N + jw\mathbf{W}_{NN} & & \end{bmatrix} \begin{bmatrix} \mathbf{I}_1 \\ \vdots \\ \mathbf{I}_K \\ \vdots \\ \mathbf{I}_N \end{bmatrix} \quad (5)$$

where  $\mathbf{M}_{1N}$  is a matrix contains every mutual inductance between the filament loops in the first and  $N_{\text{th}}$  turn, and  $\mathbf{U}_N$ ,  $\mathbf{I}_N$ , and  $\mathbf{R}_N$  are the matrices as

$$\mathbf{U}_N = [u_{N1}, \dots, u_{N_g}, \dots, u_{Nn}] \quad (6)$$

$$\mathbf{I}_N = [i_{N1}, \dots, i_{N_g}, \dots, i_{Nn}] \quad (7)$$

$$\mathbf{R}_N = \text{diag}[R_{N1}, \dots, R_{N_g}, \dots, R_{Nn}] \quad (8)$$

where  $u_{N1}$ ,  $i_{N1}$ , and  $R_{N1}$  depict the voltage, current, and dc resistance, respectively, of the first filament loop in the  $N_{\text{th}}$  turn. The overall current  $I$  in the coil is assumed to be 1 A, and the total voltage  $U$  is an unknown variable. There are

relationships as

$$I = \sum_{g=1}^n i_{1g} = \cdots = \sum_{g=1}^n i_{Kg} = \cdots = \sum_{g=1}^n i_{Ng} = 1A \quad (9)$$

$$u_N = u_{N1} = \cdots = u_{N_g} = \cdots = u_{Nn} \quad (10)$$

$$U = u_1 + \cdots u_K + \cdots u_N. \quad (11)$$

By solving (5), we can obtain matrices  $\mathbf{U}_1, \dots, \mathbf{U}_K, \dots, \mathbf{U}_N$  and  $\mathbf{I}_1, \dots, \mathbf{I}_K, \dots, \mathbf{I}_N$ , and then the impedance  $Z$  of the  $N$ -turn planar surface coil can be calculated by

$$Z = \left( \frac{\sum_{K=1}^N u_K}{i} \right) = \sum_{K=1}^N u_K, \quad i = 1A \quad (12)$$

and the ac resistance of the surface coil is

$$R = \text{Real}(Z) = \text{real} \left( \sum_{K=1}^N u_K \right). \quad (13)$$

The SNR can be further represented as

$$\text{SNR} \propto \frac{B_1}{\sqrt{R}} = \frac{\sum_{K=1}^N \sum_{g=1}^n B_{Kg}}{\sqrt{\text{real} \left( \sum_{K=1}^N u_K \right)}} \quad (14)$$

where the total effective RF magnetic field  $B_1$  is the sum of the magnetic field generated by all filament loops,  $B_{Kg}$  represents the field produced by the  $g_{\text{th}}$  filament loop in the  $K_{\text{th}}$  turn, which can be calculated via Biot-Savart law [29].

To determine the optimal coil structure, we perform a systematic study of these parameters and their impact on  $B_1$  and  $R$ . Based on these calculations, we are able to find the best combination of coil turn spacing ( $p$ ), inner diameter ( $d$ ), and the number of turns ( $n$ ) that maximizes the SNR in the target area of TMJ.

### C. Optimal Coil Selection

The coil turn spacing ( $p$ ) affects the SNR of the surface coil by altering the coil ac resistance ( $R$ ). When the turn spacing is narrow, it causes a severe proximity effect, leading to an increase in coil resistance and a decrease in SNR; however, when the turn spacing exceeds a certain value, the skin effect becomes negligible. This threshold value was determined by calculating the SNR of several coils with varying inner diameters ( $d$ ) at different turn spacings ( $p$ ). As shown in Fig. 5, the results show that normalized SNR remains stable when the turn spacing is greater than 2 mm, indicating that the proximity effect is insignificant. Based on these findings, a coil turn spacing of 2 mm is chosen.

In the study, the SNR along the  $z$ -axis and in the  $xoy$  plane were considered simultaneously. The SNR dependence on the inner diameter ( $d$ ) of the coil is illustrated in Fig. 6(a) and (b). The SNR is high close to the surface of the coil for smaller diameters, but it decreases rapidly as the distance increases, as shown in Fig. 6(a). Fig. 6(b) depicts that the coil with a 60 mm diameter offers the highest SNR and a relatively larger FOV in the  $xoy$  plane ( $z = 40$  mm); therefore, the inner diameter of the coil was fixed at 60 mm. The relationship between the SNR and the number of turns ( $n$ ) in the coil is

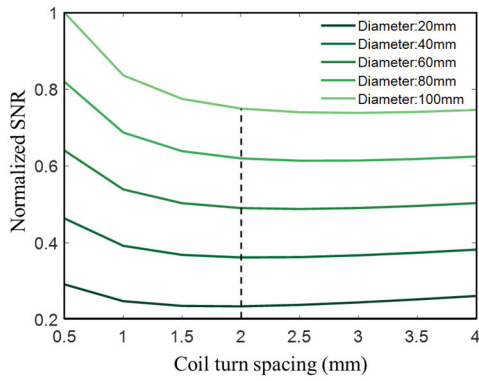


Fig. 5. Normalized resistance with coil turns spacing. The SNR is presented in the form of normalized values ranging from 0 to 1.

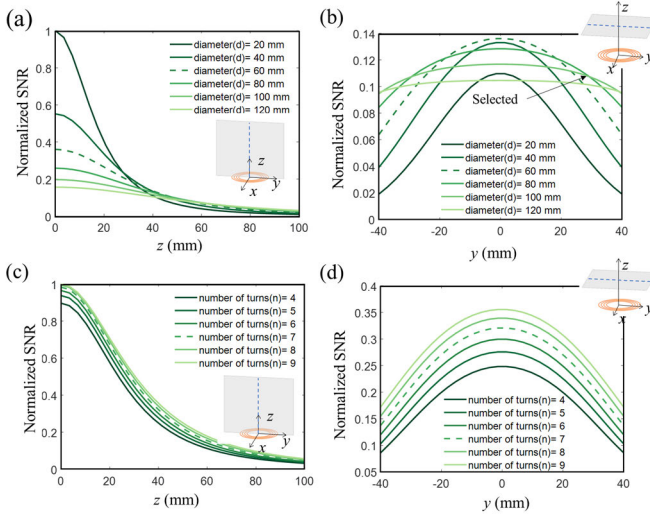


Fig. 6. Normalized SNR with inner diameter. (a) SNR along the  $z$ -axis with diameter. (b) SNR along the  $y$ -axis with diameter. (c) SNR along the  $z$ -axis with a number of turns. (d) SNR along the  $y$ -axis with a number of turns. The SNR is presented in the form of normalized values ranging from 0 to 1.

demonstrated in Fig. 6(c) and (d), showing that increasing the number of turns leads to a gradual increase in SNR, but with a diminishing rate of growth. To avoid the inconvenience of using oversized coils, a coil with seven turns was selected for the experiment.

In conclusion, a flat circular coil with an inner diameter of 60 mm, a turn spacing of 2 mm, and seven turns was ultimately chosen as the optimal solution.

#### D. Experiments

To verify the calculation results, six coils with different structures were fabricated and tested, as shown in Fig. 7. The first row shows four coils with five turns and different inner diameters (20, 40, 60, and 80 mm), while the second row shows three coils with an inner diameter of 60 mm and different numbers of turns (3, 5, and 7). Coil 6 was the calculated optimal coil. The six coils were placed on one side of a square water phantom and imaged, the results of which are shown in Fig. 8.

The SNR of the images along line 1 and line 2 were plotted in Fig. 9, which shows that coil 6 meets the design

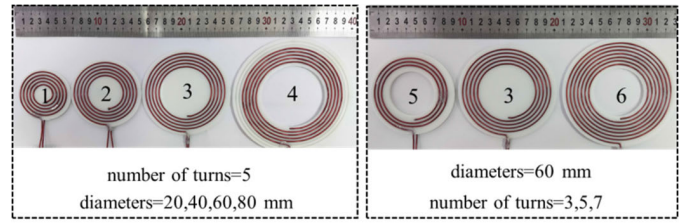


Fig. 7. Real coil structures of the six coils.

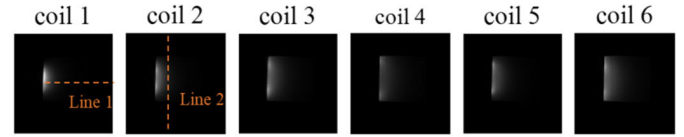


Fig. 8.  $T_1$ -weighted images of the six coils.

requirements with a high SNR in the depth range of 30–40 mm and a uniform SNR distribution in the 35 mm plane. The experimental results confirmed the calculation results. Finally, coil 6 was used for TMJ imaging.

The placement of the coil on the head surface is depicted in Fig. 10. The results of the TMJ imaging of volunteers using coil 6 can be seen in Fig. 11, which showed good imaging quality with high SNR and clear TMJ structures. The first and second rows of images are the TMJ imaging results of the volunteer with the mouth closed and open, respectively. Together, the two images in the open and closed positions can provide a diagnosis of TMJ disorder. The third row of images shows the TMJ imaging results in the oblique coronal position with the mouth closed.

Fig. 12 shows one of the  $T_1$ -weighted TMJ images and the corresponding SNR distribution map. It is evident that within undesired areas, the SNR is notably reduced. Conversely, in the desired region, there is a significantly robust SNR exhibiting a local enhancement effect. Within the TMJ region, the outer layers (cortex) of the condyle (marked with a star) and temporal bone (marked with a triangle) do not present any MRI signal ( $\text{SNR} \approx 1$ ). In contrast, their marrow demonstrates a relatively high signal intensity attributable to a higher lipid content, resulting in an SNR exceeding 15. The normal TMJ disk (marked with an arrow) maintains a biconcave shape and manifests as an area with low signal intensity, with an SNR of approximately 1. Based on the aforementioned characteristics, we can distinguish the shape and position of the disk in this image, providing a diagnostic basis for TMJ disorders.

High-field MRI is considered the gold standard [30], [31] for diagnosing TMJ disorders because it allows direct visualization of the TMJ disk (anatomical structure is shown in Fig. 2) in both the open- and closed-mouth positions. In Fig. 13, VLF MRI images were compared with high-field MRI (Siemens, Avanto, 1.5 T) images for both open- and closed-mouth positions, with the disk marked in red lines. Healthy volunteers were the imaging subjects, and it can be seen that in the open- or closed-mouth position, the disk consistently remains above the condyle. Both portable VLF and high-field imaging can distinguish the position and shape

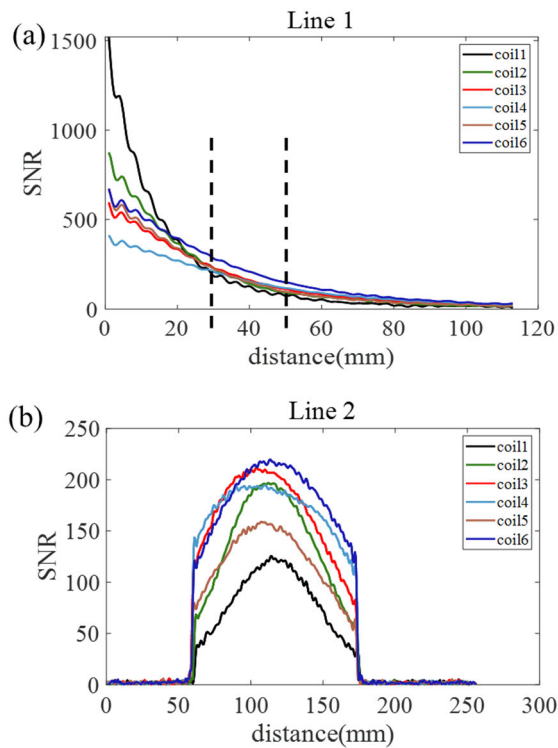


Fig. 9. Experimental SNR values (a) along line 1 and (b) along line 2 (coil 6 is the optimal coil in the calculation).

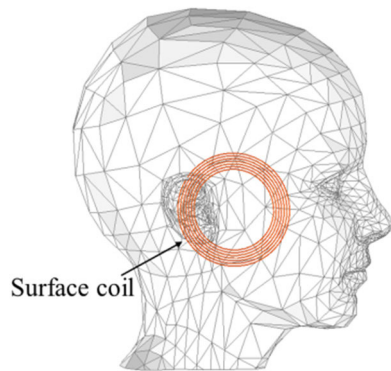


Fig. 10. TMJ surface coil placement.

of the TMJ disk, which is indicative for diagnosing TMJ disorders. Of course, VLF dental imaging is a new application, and its direct use in clinical diagnosis in hospitals requires some clinical validation over time. The imaging results, however, indicate that it indeed holds potential for dental diagnostics.

#### IV. RESONANT COIL DESIGN FOR TEETH IMAGING

##### A. Coil Design and Simulation

MRI teeth imaging requires high SNR in a small target region. The intraoral surface coil offers an obvious advantage over body coils or extraoral surface coils, but its wired connection restricts its flexibility and comfort. A low-frequency resonant coil is proposed as a replacement for the traditional intraoral surface coil. This solution allows for wireless operation and improves patient comfort.

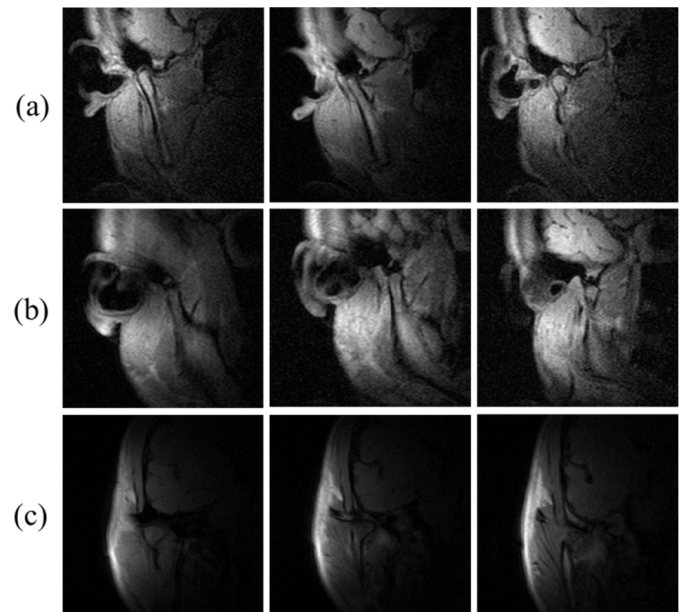


Fig. 11. TMJ  $T_1$ -weighted images of volunteers, showing the anatomy of TMJ and related muscles. (a) Closed-mouth, oblique sagittal position. (b) Open-mouth, oblique sagittal position. (c) Closed-mouth, oblique coronal position. A 3-D gradient recalled echo (GRE) sequence was utilized for  $T_1$ -weighted imaging. Slice thickness = 10 mm, echo time [TE] = 21 ms, repetition time [TR] = 46 ms, number of averages = 4, resolution =  $1.5 \times 1.5 \times 10 \text{ mm}^3$ , and FOV:  $200 \times 200 \text{ mm}$ .

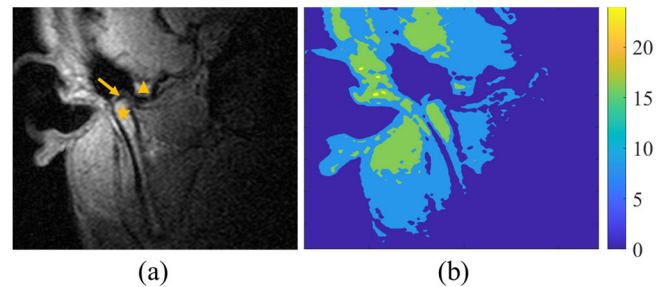


Fig. 12. TMJ imaging result analysis. (a)  $T_1$ -weighted image, including TMJ disk (arrow), temporal bone (triangle), and condyle (star). (b) SNR distribution map: SNR measures useful signal strength relative to background noise in the image.

A resonant coil, which is passive and does not require electrical power, can be used in conjunction with a head or body coil to improve the local SNR. As depicted in Fig. 14(a), the resonant coil has resistance ( $R_1$ ) and inductance ( $L_1$ ), and chip capacitors ( $C_2$ ) connected to its ends. When NMR signals at 2.32 MHz are detected, the presence of capacitors leads to a series resonance in the coil, resulting in the coil exhibiting low impedance and high resonant current. As shown in Fig. 14(b), the resonant coil and the head receiving coil are positioned parallel to each other, which are related in the form of mutual inductance. The locally enhanced magnetic resonance signal is then captured using the solenoidal RF receiving coil. In order to evaluate the SNR enhancement effects, the head receiving coil can be used as the excitation source, and its magnetic field intensity is used to gauge its sensitivity. The resonant coil reaches resonance under the excitation of the head receiving coil, which leads to a sharp increase in the resonant current and magnetic field.

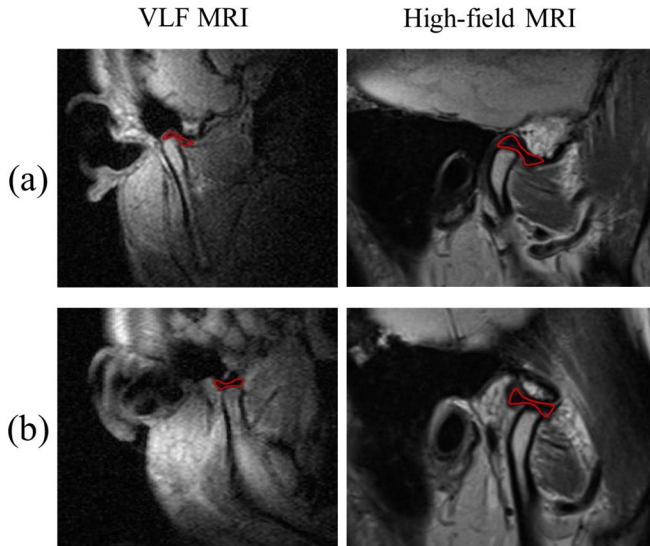


Fig. 13. TMJ image comparison between VLF MRI (50 mT) and high-field MRI (Siemens, Avanto, 1.5 T) devices. The structure marked with red lines is a disk of TMJ. (a) Closed-mouth, oblique sagittal position. (b) Open-mouth, oblique sagittal position.

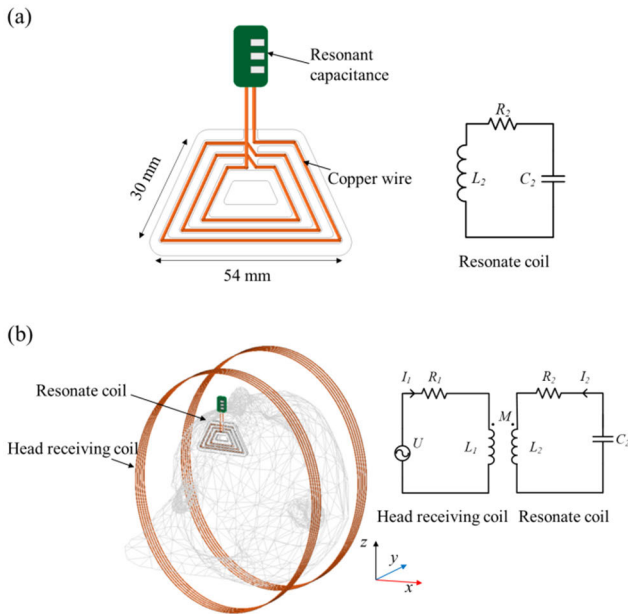


Fig. 14. Coil models and corresponding circuit diagrams. (a) Resonant coil and its equivalent circuit. (b) Head receiving coil and resonant coil are related in the form of mutual inductance.

The resonance effect results in a significant increase in the SNR of the receiving coil. According to the circuit diagram in Fig. 14(b), we have

$$R_1 I_1 + j\omega L_1 I_1 + j\omega M I_2 = U \quad (15)$$

$$R_2 I_2 + j\omega L_2 I_2 + \frac{1}{j\omega C_2} I_2 + j\omega M I_1 = 0 \quad (16)$$

where  $R_1$ ,  $R_2$ ,  $L_1$ , and  $L_2$  denote the resistances and inductances of the head receiving coil and the resonant coil,  $U$  is the unit voltage across the head receiving coil,  $M$  denotes the mutual inductance,  $C_2$  is the lumped capacitance added to the ports of the resonant coil. When the resonant coil is in

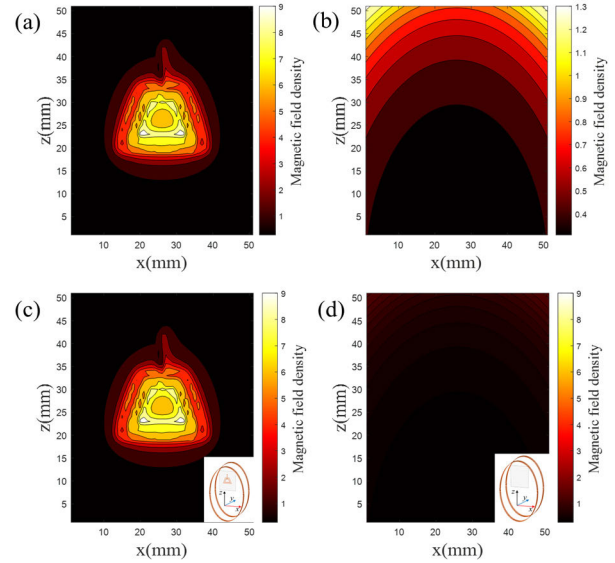


Fig. 15. Magnetic field distribution from FEM simulation, where (a) and (c) represent the condition with the resonant coil, and (b) and (d) represent the condition with only the head receiving coil. (a) and (b) are shown in different color scales, while (c) and (d) share the same color scale.

resonance, we have

$$j\omega L_2 + \frac{1}{j\omega C_2} = 0. \quad (17)$$

Then, the current in the head receiving coil  $I_1$  and resonant coil  $I_2$  can be expressed by

$$I_1 = \frac{R_2}{\omega^2 M^2 + (R_1 + j\omega L_1) R_2} \quad (18)$$

$$I_2 = -\frac{j\omega M}{\omega^2 M^2 + (R_1 + j\omega L_1) R_2}. \quad (19)$$

The equivalent magnetic field is the superposition of the field produced by  $I_1$  and  $I_2$ .

FEM Simulations were carried out to show the enhancement effects of the resonant coil. The voltage of unit magnitude was added to the ports of the head receiving coil, generating an RF magnetic field in the image region. The distribution of the RF magnetic field reflects the sensitivity of the receiving coil. As shown in Fig. 15, the simulation results illustrate that the resonant coil significantly enhances the magnetic field compared to the scenario with only the head receiving coil.

### B. Coil Construction

As indicated by the analysis, the resonant coil has the capacity to enhance the local SNR in a manner similar to the intraoral surface coil. To make a comparison between the two, imaging studies were conducted using the same water phantom. Two trapezoidal spiral flat coils were fabricated and used as the intraoral RF surface coil and the resonant coil, as shown in Fig. 16(a) and (b), respectively. The resistance and inductance for trapezoidal spiral flat coils is 58 m $\Omega$  and 347 nH. The intraoral RF surface coil had a  $\pi$ -shaped circuit added for matching it to 50  $\Omega$ , and the measured transmission coefficient was 25 dB. The resonant coil had added chip capacitors to make it resonant at the desired frequency, and the

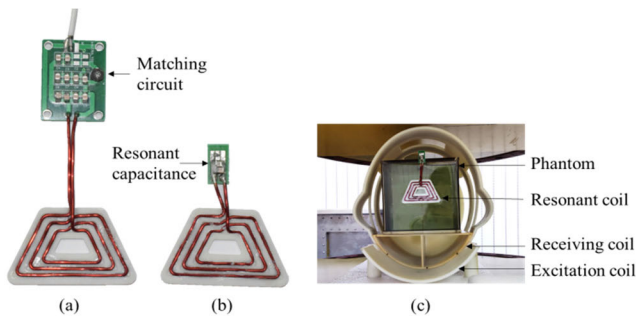


Fig. 16. Intraoral surface coil, resonant coil, and experiment setup. (a) Intraoral surface coil, connected to the signal line with the matching circuit. (b) Resonant coil, with its resonant capacitances. (c) Water phantom imaging experiment setup for resonant coil (for intraoral surface coil, the setup is the same, but the head receiving coil is removed).

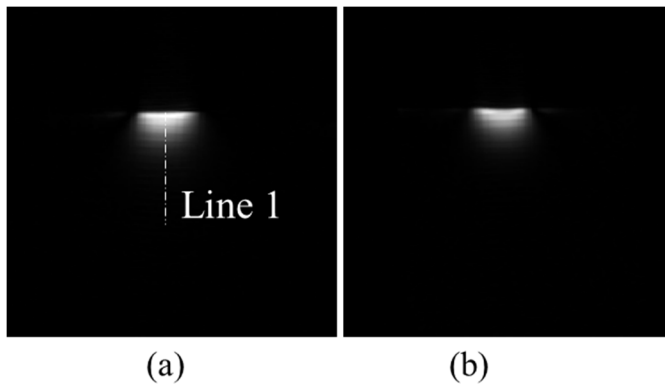


Fig. 17.  $T_1$ -weighted images of the water phantom, with (a) intraoral surface coil and (b) resonant coil.

actual matching capacitance of the resonant coil is 13 540 pF. The rectangular water phantom has a side length of 110 mm, and its solution is composed of copper sulfate pentahydrate ( $\text{CuSO}_4 \cdot 5\text{H}_2\text{O}$ ) and pure water ( $\text{H}_2\text{O}$ ) with a ratio of 1.95 g/L. As shown in Fig. 16(c), the phantom is placed in the center of the solenoid receiving coil, and the resonant coil is placed on the center surface of the phantom. The setup was the same for the imaging experiment of the intraoral surface coil; however, the head receiving coil was not working at that time. The  $T_1$ -weighted images of a water phantom using these two coils are shown in Fig. 17, with a comparison of SNR values along line 1 in Fig. 18. This comparison is based on the very best performances ever achieved by the two coils. The imaging findings demonstrated that the resonant coil and intraoral surface can achieve a similar SNR performance. It was discovered that the resonant coil had a more user-friendly construction and was wireless, making it more practical to employ in situations where plug-in coils are necessary.

### C. Teeth and Periodontal Apparatus Imaging

The resonant coil with the head receiving coil was used for teeth imaging.  $T_1$ -weighted images are shown in Fig. 19. The results demonstrate that the resonant coil enhances the SNR effectively in the tooth region while exhibiting a low signal in the rest of the head area. The  $T_1$ -weighted image of the tooth

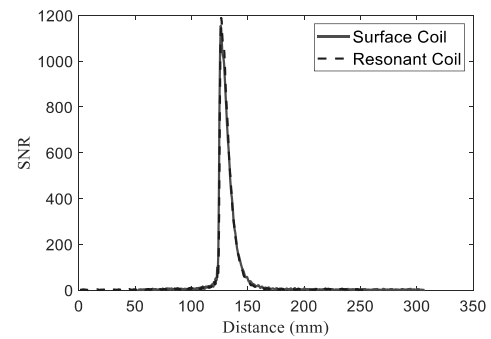


Fig. 18. SNR comparison along line 1 between the intraoral surface coil and the resonant coil.

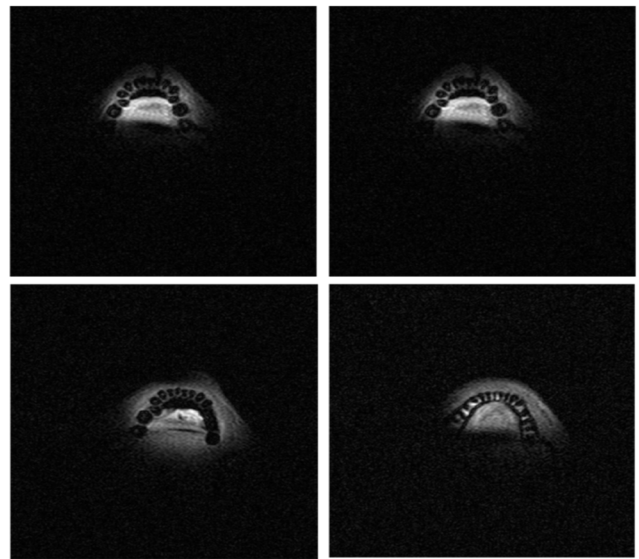


Fig. 19.  $T_1$ -weighted images of the teeth and periodontal apparatus of volunteers. 3-D GRE sequence was utilized for  $T_1$ -weighted imaging. These images were acquired in 1 min 30 s, with a slice thickness of 8 mm. Echo time [TE] = 19 ms, repetition time [TR] = 40 ms, number of averages = 4, resolution =  $1.5 \times 1.5 \times 10 \text{ mm}^3$ , and FOV:  $200 \times 200 \text{ mm}$ .

displays the bone with a low signal intensity, while the pulp exhibits a high signal intensity.

SNR analysis is carried out in the desired region in the teeth imaging result, as shown in Fig. 20. The highest SNR is observed in the tongue region (marked with a triangle, maximum SNR > 20). This is because the resonant coil is closest to the tongue, and the tongue contains abundant moisture. Following that is the gingiva (marked with a star), with an SNR of around 10. The bony part of teeth typically appears as regions with low signal intensity in MRI (in this image, SNR  $\approx 1$ ). This is because dense bone tissue contains minimal water content, resulting in a relatively small contribution to the NMR signal; however, the gingival contour clearly delineates the shapes of the teeth. Additionally, the dental pulp (marked with an arrow) within the teeth also exhibits intermediate signal intensity (SNR  $\approx 5$ ), allowing for a preliminary assessment of the morphology of the dental pulp through this image. Overall, the imaging results align with our design specifications. The intraoral resonant coil successfully

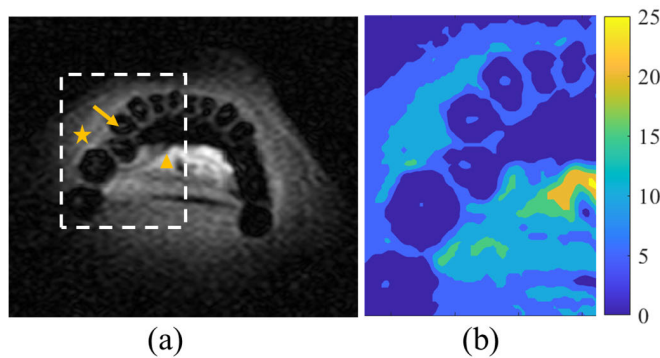


Fig. 20. Teeth imaging result analysis. (a)  $T_1$ -weighted image, including dental pulp (arrow), tongue (triangle), and gingival (star). (b) Local SNR distribution calculated by dividing the useful signal by the background noise.

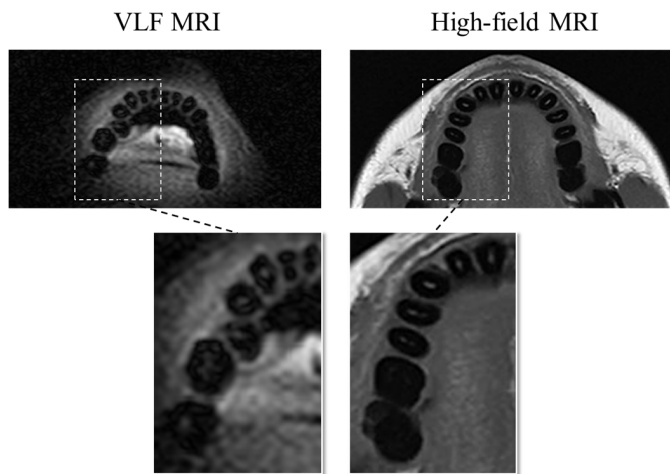


Fig. 21. Teeth image comparison between the VLF MRI (50 mT) and high-field MRI (Siemens, Avanto, 1.5 T) devices.

enhances local SNR, displaying low signals in undesired areas, such as the cheeks, while revealing signals in the tooth region.

We also compared the VLF MRI dental images with high-field MRI images, as shown in Fig. 21. In the high-field (Siemens, Avanto, 1.5 T) imaging results using the traditional coil (head coil), there is a uniform SNR throughout the entire image. In contrast, our proposed resonant coil only enhances the SNR in the dental area, avoiding the undesired high signal in the cheek area. In both VLF and high-field MRI imaging results, the structural contours of the teeth and dental pulp can be distinguished. Compared to high-field imaging results, the SNR and resolution in low-field imaging are inevitably weaker; however, this is a compromise in exchange for equipment size, portability, and cost-effectiveness.

## V. CONCLUSION

This study provides insights into the design and implementation of a VLF MRI system for dental imaging, specifically focusing on the optimization of the surface coil for TMJ imaging and the use of a wireless resonant coil for intraoral imaging. The results of the imaging experiments on phantom and in vivo subjects demonstrate the capability of the system to capture images of the TMJ and teeth. The presented results are

valuable for the development of advanced VLF MRI systems for dental imaging applications.

The principle of MRI dictates that a higher magnetic field strength can lead to better image quality; therefore, inevitably, reducing the size and weight of the magnet weakens the image quality; however, due to the demand for portable MRI in some special fields, a trade-off between image quality and portability is necessary to meet various usage requirements. The benefits derived from portability include.

- 1) *Accessibility*: Low-cost, portable MRI scanners can increase access to MRI technology in underserved areas, smaller clinics, or remote locations where traditional MRI machines might not be feasible.
- 2) *Ease of Installation*: Portable scanners are generally easier to install and set up compared to high-field MRI systems; for example, no cooling device is needed.
- 3) *Point-of-Care Imaging*: Portable MRI scanners can be used for point-of-care imaging, enabling rapid diagnosis in different scenarios or providing real-time imaging during surgical procedures.

Accordingly, portability brings some cons, including:

- 1) *Low Image Quality*: Portable MRI scanners may have limitations in terms of image quality compared to high-field scanners. It will take some time to accumulate rigorous certification before it can be used in real clinical settings.
- 2) *Insufficient Stability*: While the equipment does not require a cooling system, the permanent magnet can be lightly influenced by external temperatures. As a result, the uniformity of the static magnetic field is affected, thereby causing unstable performance.

In the future, there will be a heightened focus on enhancing the image quality of portable MRI scanners. This will involve advancements in RF technology and the exploration of innovative magnet structures. Additionally, research into effective temperature control systems for permanent magnets will be conducted.

## APPENDIX

The technical specifications of the proposed MRI scanner are given as follows.

- 1) *Structural Information*: The system stands 90 cm wide, 110 cm high, and weighs 600 kg. No cooling is required, and it can be installed in an average-sized room.
- 2) *Portability*: Assistive wheels can be added, allowing a single person to move it between rooms.
- 3) *Static Magnetic Field*: Generated by the SmCo permanent magnet. The average magnetic field strength in the ROI (sphere with a diameter of 200 mm) is 50 mT, with a nonuniformity of less than 200 ppm.
- 4) *Gradient Field*: Passive gradient shielding systems are installed. The maximum nonlinearity is 4.5% ( $X/Y$  gradient coil) and 3.2% ( $Z$  gradient coil) for full ROI, and can achieve a maximum gradient strength of  $242 \mu\text{T}/(\text{m}\cdot\text{A})$  ( $X/Y$  gradient coil) and  $274 \mu\text{T}/(\text{m}\cdot\text{A})$  ( $Z$  gradient coil).

- 5) *RF Coils*: Equipped with surface coils for TMJ imaging and intraoral resonant coils for dental imaging. Head volume coils are provided as a supplement.
- 6) *Pulse Sequences*:  $T_1$ -weighted,  $T_2$ -weighted, and diffusion-weighted are available.
- 7) *Imaging Time*: The imaging time depends on the selected imaging parameters. For  $T_1$ -weighted imaging, the typical imaging time is 2.5 min for 12 slices.

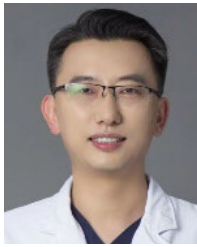
## REFERENCES

- [1] N. K. Kumar, S. Merwade, P. Prabakaran, C. H. L. Priya, B. S. Annapoorna, and C. N. Guruprasad, "Magnetic resonance imaging versus cone beam computed tomography in diagnosis of periapical pathosis—A systematic review," *Saudi Dental J.*, vol. 33, no. 8, pp. 784–794, Dec. 2021, doi: [10.1016/j.sdentj.2021.09.010](https://doi.org/10.1016/j.sdentj.2021.09.010).
- [2] T. Nakamura, "Dental MRI: A road beyond CBCT," *Eur. Radiol.*, vol. 30, no. 12, pp. 6389–6391, Sep. 2020, doi: [10.1007/s00330-020-07321-7](https://doi.org/10.1007/s00330-020-07321-7).
- [3] T. Hilgenfeld et al., "Use of dental MRI for radiation-free guided dental implant planning: A prospective, in vivo study of accuracy and reliability," *Eur. Radiol.*, vol. 30, no. 12, pp. 6392–6401, Sep. 2020, doi: [10.1007/s00330-020-07262-1](https://doi.org/10.1007/s00330-020-07262-1).
- [4] M. Zidan et al., "Endodontic working length measurements of premolars and molars in high-resolution dental MRI: A clinical pilot study for assessment of reliability and accuracy," *Clin. Oral Invest.*, vol. 26, no. 11, pp. 6765–6772, Jul. 2022, doi: [10.1007/s00784-022-04636-1](https://doi.org/10.1007/s00784-022-04636-1).
- [5] O. Tymofiyeva, K. Rottner, P. M. Jakob, E.-J. Richter, and P. Proff, "Three-dimensional localization of impacted teeth using magnetic resonance imaging," *Clin. Oral Invest.*, vol. 14, no. 2, pp. 169–176, Apr. 2009, doi: [10.1007/s00784-009-0277-1](https://doi.org/10.1007/s00784-009-0277-1).
- [6] T. Hilgenfeld et al., "Use of dental MRI for radiation-free guided dental implant planning: A prospective, in vivo study of accuracy and reliability," *Eur. Radiol.*, vol. 30, no. 12, pp. 6392–6401, Sep. 2020, doi: [10.1007/s00330-020-07262-1](https://doi.org/10.1007/s00330-020-07262-1).
- [7] Z. Yang et al., "Magnetic resonance imaging (MRI) evaluation for anterior disc displacement of the temporomandibular joint," *Med. Sci. Monitor*, vol. 23, pp. 712–718, Feb. 2017, doi: [10.12659/msm.899230](https://doi.org/10.12659/msm.899230).
- [8] X. Tomas et al., "MR imaging of temporomandibular joint dysfunction: A pictorial review," *RadioGraphics*, vol. 26, no. 3, pp. 765–781, May 2006, doi: [10.1148/rg.263055091](https://doi.org/10.1148/rg.263055091).
- [9] X. Kong et al., "Gradient coil design method specifically for permanent-magnet-type low field portable MRI brain scanner," *IEEE Trans. Instrum. Meas.*, vol. 72, pp. 1–12, 2023, doi: [10.1109/TIM.2022.3225042](https://doi.org/10.1109/TIM.2022.3225042).
- [10] S. Shen et al., "An optimized quadrature RF receive coil for very-low-field (50.4 mT) magnetic resonance brain imaging," *J. Magn. Reson.*, vol. 342, Sep. 2022, Art. no. 107269, doi: [10.1016/j.jmr.2022.107269](https://doi.org/10.1016/j.jmr.2022.107269).
- [11] M. H. Mazurek et al., "Portable, bedside, low-field magnetic resonance imaging for evaluation of intracerebral hemorrhage," *Nature Commun.*, vol. 12, no. 1, p. 5119, Aug. 2021, doi: [10.1038/s41467-021-25441-6](https://doi.org/10.1038/s41467-021-25441-6).
- [12] M. Sarracanie, C. D. LaPierre, N. Salameh, D. E. J. Waddington, T. Witzel, and M. S. Rosen, "Low-cost high-performance MRI," *Sci. Rep.*, vol. 15, no. 5, p. 15177, Oct. 2015, doi: [10.1038/srep15177](https://doi.org/10.1038/srep15177).
- [13] T. C. Arnold, C. W. Freeman, B. Litt, and J. M. Stein, "Low-field MRI: Clinical promise and challenges," *J. Magn. Reson. Imag.*, vol. 57, no. 1, pp. 25–44, Jan. 2023, doi: [10.1002/jmri.28408](https://doi.org/10.1002/jmri.28408).
- [14] J. Gradl et al., "Application of a dedicated surface coil in dental MRI provides superior image quality in comparison with a standard coil," *Clin. Neuroradiol.*, vol. 27, no. 3, pp. 371–378, Feb. 2016, doi: [10.1007/s00062-016-0500-9](https://doi.org/10.1007/s00062-016-0500-9).
- [15] Z. Chen, K. Solbach, D. Erni, and A. Rennings, "Improving  $B_1$  efficiency and signal-to-noise-ratio of a surface coil by a high-impedance-surface RF shield for 7-T magnetic resonance imaging," *IEEE Trans. Microw. Theory Techn.*, vol. 65, no. 3, pp. 988–997, Mar. 2017, doi: [10.1109/tmtt.2016.2631169](https://doi.org/10.1109/tmtt.2016.2631169).
- [16] A. Manoliu et al., "Comparison of a 32-channel head coil and a 2-channel surface coil for MR imaging of the temporomandibular joint at 3.0 T," *Dentomaxillofacial Radiol.*, vol. 45, no. 4, Apr. 2016, Art. no. 20150420, doi: [10.1259/dmfr.20150420](https://doi.org/10.1259/dmfr.20150420).
- [17] A. C. Özen et al., "Design of an intraoral dipole antenna for dental applications," *IEEE Trans. Biomed. Eng.*, vol. 68, no. 8, pp. 2563–2573, Aug. 2021, doi: [10.1109/TBME.2021.3055777](https://doi.org/10.1109/TBME.2021.3055777).
- [18] A.-K. Bracher et al., "Ultrashort echo time (UTE) MRI for the assessment of caries lesions," *Dentomaxillofacial Radiol.*, vol. 42, no. 6, Jun. 2013, Art. no. 20120321, doi: [10.1259/dmfr.20120321](https://doi.org/10.1259/dmfr.20120321).
- [19] O. Tymofiyeva et al., "In vivo MRI-based dental impression using an intraoral RF receiver coil," *Concepts Magn. Reson. B, Magn. Reson. Eng.*, vol. 33B, no. 4, pp. 244–251, Oct. 2008, doi: [10.1002/cmr.b.20126](https://doi.org/10.1002/cmr.b.20126).
- [20] D. Idiyattullin, C. Corum, S. Moeller, H. S. Prasad, M. Garwood, and D. R. Nixdorf, "Dental magnetic resonance imaging: Making the invisible visible," *J. Endodontics*, vol. 37, no. 6, pp. 745–752, Jun. 2011, doi: [10.1016/j.joen.2011.02.022](https://doi.org/10.1016/j.joen.2011.02.022).
- [21] D. Idiyattullin, C. A. Corum, D. R. Nixdorf, and M. Garwood, "Intraoral approach for imaging teeth using the transverse b 1 field components of an occlusally oriented loop coil," *Magn. Reson. Med.*, vol. 72, no. 1, pp. 160–165, Jul. 2014, doi: [10.1002/mrm.24893](https://doi.org/10.1002/mrm.24893).
- [22] U. Ludwig et al., "Dental MRI using wireless intraoral coils," *Sci. Rep.*, vol. 6, no. 1, Mar. 2016, Art. no. 23301, doi: [10.1038/srep23301](https://doi.org/10.1038/srep23301).
- [23] S. Wright and L. Wald, "Theory and application of array coils in MR spectroscopy," *NMR Biomed.*, vol. 10, no. 8, pp. 394–410, Dec. 1998, doi: [10.1002/\(SICI\)1099-1492\(199712\)10:8<394::AID-NBM494>3.0.CO;2-0](https://doi.org/10.1002/(SICI)1099-1492(199712)10:8<394::AID-NBM494>3.0.CO;2-0).
- [24] S. Shen, Z. Xu, N. Koonjoo, and M. S. Rosen, "Optimization of a close-fitting volume RF coil for brain imaging at 6.5 mT using linear programming," *IEEE Trans. Biomed. Eng.*, vol. 68, no. 4, pp. 1106–1114, Apr. 2021, doi: [10.1109/TBME.2020.3002077](https://doi.org/10.1109/TBME.2020.3002077).
- [25] D. H. Kim and Y. J. Park, "Calculation of the inductance and AC resistance of planar rectangular coils," *Electron. Lett.*, vol. 52, no. 15, pp. 1321–1323, Jul. 2016, doi: [10.1049/el.2016.0696](https://doi.org/10.1049/el.2016.0696).
- [26] I. Hetita, D. A. Mansour, Y. Han, P. Yang, and A. S. Zalfaf, "Experimental and numerical analysis of transient overvoltages of PV systems when struck by lightning," *IEEE Trans. Instrum. Meas.*, vol. 71, pp. 1–11, 2022, doi: [10.1109/TIM.2022.3199225](https://doi.org/10.1109/TIM.2022.3199225).
- [27] P. Scholz, "Analysis and numerical modeling of inductively coupled antenna systems," Tech. Rep., 2010.
- [28] C. Akyel, S. Babic, and S. Kincic, "New and fast procedures for calculating the mutual inductance of coaxial circular coils (circular coil-disk coil)," *IEEE Trans. Magn.*, vol. 38, no. 5, pp. 2367–2369, Sep. 2002, doi: [10.1109/TMAG.2002.803576](https://doi.org/10.1109/TMAG.2002.803576).
- [29] J. Simpson, J. Lane, C. Immer, and R. Youngquist, "Simple analytic expressions for the magnetic field of a circular current loop," NASA Tech. Rep. Server (NTRS) Collection, Tech. Rep., Jan. 2003, doi: <https://ntrs.nasa.gov/citations/20010038494>.
- [30] Z. Yang et al., "Magnetic resonance imaging (MRI) evaluation for anterior disc displacement of the temporomandibular joint," *Med. Sci. Monitor, Int. Med. J. Exp. Clin. Res.*, vol. 23, pp. 712–718, Feb. 2017, doi: [10.12659/msm.899230](https://doi.org/10.12659/msm.899230).
- [31] Y. Zhu, C. Zheng, Y. Deng, and Y. Wang, "Arthroscopic surgery for treatment of anterior displacement of the disc without reduction of the temporomandibular joint," *Brit. J. Oral Maxillofacial Surg.*, vol. 50, no. 2, pp. 144–148, Mar. 2012, doi: [10.1016/j.bjoms.2011.02.004](https://doi.org/10.1016/j.bjoms.2011.02.004).



**Xiaohan Kong** received the B.Sc. and M.Sc. degrees from Chongqing University, Chongqing, China, in 2016 and 2020, respectively.

Her research interests include computational electromagnetism, design optimization of electromagnetic structures, and very low-field (VLF) magnetic resonance imaging (MRI).



**Yaomin Zhu** was born in Liaoning, China, in 1977. He received the Ph.D. degree from China Medical University, Liaoning, China, in 2005.

He is currently an Honor Professor and Director of the Shenzhen Stomatology Hospital, Shenzhen, China. His research focuses on stomatology, especially in maxillofacial surgery, temporomandibular joint surgery, facial plastic surgery, and orthognathic surgery.



**Yucheng He** received the Ph.D. degree in electric engineering from Chongqing University, Chongqing, China, in 2020.

Currently engaged in Postdoctoral Research at Shenzhen Aerospace Science and Technology Innovation Institute, Shenzhen, China. His research interest includes magnetic resonance imaging (MRI) imaging methods and radio frequency (RF) coil designing methods.



**Sheng Shen** was born in Anhui, China, in 1993. He received the B.Sc. degree from Liaoning University, Liaoning, China, in 2016, and the Ph.D. degree from Chongqing University, Chongqing, China, in 2021.

He is currently a Postdoctoral Research Fellow at Massachusetts General Hospital/Martinos Center and Harvard Medical School, Boston, MA, USA. His research interests include electromagnetic calculation, sensor technologies, magnetic resonance physics, and very low-field (VLF) magnetic resonance imaging (MRI).



**Mingjian Hong** received the B.Sc. degree in applied mathematics, the M.Sc. degree in operations research and control theory, and the Ph.D. degree in instrument science and technology from Chongqing University, Chongqing, China, in 1999, 2002, and 2011, respectively.

He is currently an Associate Professor at the School of Big Data and Software Engineering, Chongqing University. His research interests include machine learning and artificial intelligence applications.



**Jiamin Wu** received the Ph.D. degree in electric engineering from Chongqing University, Chongqing, China, in 2019.

Currently engaged in Postdoctoral Research at Shenzhen Aerospace Science and Technology Innovation Institute, Shenzhen, China. His research interest includes electromagnetic field calculation, magnetic resonance imaging (MRI), and magnet designing for MRI.



**Zheng Xu** was born in Jiangsu, China, in 1980. He received the B.Sc., M.Sc., and Ph.D. degrees in electrical engineering from Chongqing University, Chongqing, China, in 2002, 2005, and 2008, respectively.

He is currently a Professor with the School of Electrical Engineering, Chongqing University. His research areas include designing the magnet structure and radio frequency (RF) coil for the nuclear magnetic resonance (NMR)/magnetic resonance imaging (MRI) system.